PAPER

Check for updates

Application of single-atom Ti-doped g-C₃N₄ in photocatalytic H₂O₂ production†

Tinglei Wang,[a] Jiayu Xin,[a] Zhen Li,[a] Yong Fan [ID] *[b] and Yu Wang [ID] *[a]

Synthesizing highly effective photocatalysts for hydrogen peroxide (H_2O_2) generation is still a challenge. In this work, the doping of graphite carbon nitride nanosheets with single-atom titanium, using $TiCl_3$ as a precursor, to form single Ti atom-doped graphitic carbon nitride (Ti-SAC/g-C_3N_4) photocatalysts can efficiently address this challenge. The photocatalytic activity is enhanced by increasing the concentration of titanium to 0.09%, and subsequently decreases with further increases in the concentration of titanium, thus confirming that the concentration of titanium atoms can modulate the performance of the single-atom catalysts. Furthermore, an in-depth investigation indicates that the bottom of the conduction band (CB) and the maximum of the valence band (VB) can be controlled by varying the concentration of titanium atoms. A high bottom of the CB is beneficial to increase the photocatalytic efficiency. Under acidic conditions and utilizing sacrificial agents, the H_2O_2 production rate of Ti-C_3N_4-100 can reach 356.45 μmol L^{-1} h^{-1} and is 2.44 and 2.13 times higher than that of BCN and g-C_3N_4, respectively. The electron spin resonance (ESR) spectra suggest that the generation of superoxide radicals is crucial in the photocatalytic process. This work provides a distinctive strategy to realize single titanium atom doping and offers new insights into structure–property relationships.

1. Introduction

Hydrogen peroxide (H_2O_2), a multifunctional oxidant, has been widely used in organic synthesis, bleaching, disinfection, environmental treatment and fuel cells due to its low cost and excellent eco-friendly properties.[1–6] In general, there are two methodologies that have been employed to prepare H_2O_2. One is the anthraquinone oxidation (AO) method, which can manufacture H_2O_2 *via* Pd-catalysed cyclic hydrogenation and oxidation of alkyl-anthraquinones in organic solvents.[7] However, the process is energy intensive and causes environmental pollution, thus seriously limiting its adoption.[8,9] The second method uses photocatalytic techniques, which can sustainably convert solar energy to chemical energy without excess energy consumption and is an excellent alternative to the AO method.[10] The key to success with photocatalytic H_2O_2 synthesis is to obtain highly efficient photocatalysts. Of these photocatalysts, graphitic carbon nitride (g-C_3N_4) has attracted extensive attention.[11] Although g-C_3N_4 catalysts can constantly produce H_2O_2 by taking advantage of visible light, the low production

rate and amounts obtained, due to its low carrier separation efficiency, immensely restrict the large-scale application of g-C_3N_4.[12,13]

Recently, single atom-doped C_3N_4 photocatalysts have been investigated for enhanced photocatalytic performance.[14] For instance, Zhang *et al.* synthesized single-atom Pt/C_3N_4 and found, using synchronous illumination X-ray photoelectron spectroscopy, that the Pt–N bond was cleaved to form Pt^0 and a C=N bond under light irradiation.[15] Xiao *et al.* embedded single atom Cu into a C_3N_4 matrix and the Cu–N_x species were found to immensely improve in-plane and interlayer separation transfer of charge carriers, resulting in an increase of the photocatalytic efficiency.[16] Wang *et al.* prepared monatomic Ag dispersed mesoporous g-C_3N_4 to improve bisphenol A (BPA) degradation efficiency by utilizing the synergistic effect between silver and mesoporous g-C_3N_4.[17] Titanium-doped photocatalysts, such as titanium dioxide[18,19] and titanium carbide,[20,21] are widely applied in photocatalysis due to their wide bandgaps. Indeed, the 3d orbitals of titanium are very helpful for reduction reactions due to their high energy, which is beneficial for the production of H_2O_2. Meanwhile, the photocatalytic activity of g-C_3N_4 for H_2O_2 preparation is also low owing to the high recombination rate and low electrical conductivity. Therefore, doping single titanium atoms into g-C_3N_4 is significant, to not only enhance the position of the bottom of the conduction band to reduce the recombination rate, but also to improve the electrical conductivity. However,

[a] *State Key Laboratory of Inorganic Synthesis and Preparative Chemistry, College of Chemistry, Jilin University, 2699 Qianjin Street, Changchun 130012, P. R. China. E-mail: wangyu@jlu.edu.cn*

[b] *College of Chemistry, Jilin University, Changchun 130012, P. R. China. E-mail: mrfy@jlu.edu.cn*

the synthesis of single titanium atom-doped C_3N_4 is rarely reported because the titanium precursor easily forms TiO_2 during the reaction process. Therefore, it is highly desirable to synthesize a single titanium atom-doped C_3N_4 photocatalyst and investigate the relationship between the photocatalytic performance and the concentration of titanium atoms.

Herein, single titanium atom-doped graphitic carbon nitride catalysts have been synthesized by assembling melamine, cyanuric acid and $TiCl_3$. Single titanium atoms can be successfully embedded in the graphic C_3N_4 matrix using $TiCl_3$ as the precursor due to its excellent chemical stability in solution. The photocatalytic activity exhibits a volcanic distribution in relation to the titanium concentration. The Ti-C_3N_4-100 sample, with 0.09% titanium content, exhibits the best catalytic performance. The H_2O_2 production rate of Ti-C_3N_4-100 can reach 356.45 μmol L^{-1} h^{-1} and is 2.44 and 2.13 times higher than that of BCN and g-C_3N_4, respectively. The mechanistic investigation indicates that the bottom of the conduction band (CB) and the maximum of the valence band (VB) can be controlled by altering the concentration of titanium atoms, and that Ti-C_3N_4-100 possesses the highest bottom of the CB and maximum of the VB. The more negative the bottom of the CB is, the better the photocatalytic efficiency is. This result demonstrates that the superoxide radical can be easily generated when the bottom of the CB is negative and the generation of the superoxide radical is crucial in the photocatalytic process. This work provides a distinctive strategy to realize single atom doping of titanium and offers new insight into structure–property relationships.

2. Experimental

2.1. Chemicals

All chemicals were obtained from commercial suppliers and used without further purification. Melamine (MA, 99%), cyanuric acid (CA, 98%), 1,4-benzoquinone (BQ, 99%), and titanium chloride solution ($TiCl_3$, 15–20%) were purchased from Aladdin Biochemical Technology co, Ltd (Shanghai, China). Isopropyl alcohol (IPA, 99.7%) was purchased from TianTai co, Ltd (Tianjin, China), potassium hydrogen phthalate and potassium iodide were purchased from BeiHua co, Ltd (Beijing, China).

2.2. Synthesis of photocatalysts

2.2.1. Synthesis of bulk carbon nitride (BCN). The BCN sample was synthesized by thermal polymerization of melamine. Typically, 1 g of melamine was heated in a quartz boat with a ramp rate of 5 °C min^{-1} in an air atmosphere at 600 °C for 2 h.

2.2.2. Synthesis of graphite carbon nitride (g-C_3N_4). Melamine (20.40 g) and cyanuric acid (20.00 g) at a ratio of 1:1 were mixed and dispersed in deionized water (400 mL) and stirred for 12 hours at 70 °C in a water bath. The obtained mixture was heated in an oven at 70 °C for 36 hours to prepare the precursors. The obtained precursors were thoroughly ground

and placed in crucibles, wrapped with tin foil, and placed in a muffle furnace. Subsequently, the above-mentioned precursors were heated to 600 °C at a rate of 5 °C min^{-1} for 2 hours to obtain a light yellow powder.

2.2.3. Synthesis of single atom Ti dispersed carbon nitride (Ti-C_3N_4). The preparation of the supramolecular precursors is consistent with the above section 2.0 g of the precursor was adequately dispersed in deionized water by stirring for 30 minutes. Then, 50 μL, 100 μL, and 250 μL of $TiCl_3$ solution were mixed with a solution of the precursor and stirred for 12 hours. Subsequently, the obtained mixtures were centrifuged, washed twice with deionized water, and dried. Finally, the obtained white powders were transferred into a crucible and heated at 600 °C in a muffle furnace for 2 hours at a rate of 5 °C min^{-1}. The obtained samples were named as Ti-C_3N_4-50, Ti-C_3N_4-100, and Ti-C_3N_4-250, respectively.

2.3. Characterization

X-ray diffraction (XRD) patterns were collected using a RigakuD/Max 2550 X-ray diffractometer (Cu Kα radiation, λ = 1.5406 Å). The surface morphologies were characterized using scanning electron microscopy (SEM) conducted with a JSM-7800F field emission scanning electron microscope at an accelerating voltage of 3 kV. Transmission electron microscopy (TEM) was conducted on a FEI Tecnai G2S-Twin with a field emission gun operating at 200 kV. An FEI-Titan Cubed Themis G2 300 with a spherical aberration corrector working at 300 kV was used to record high angle annular darkfield scanning transmission electron microscopy (HAADF-STEM) and energy-dispersive spectroscopy (EDS) images. Fourier-transform infrared (FTIR) spectra were recorded in the range of 400–4000 cm^{-1} using an IFS-66V/S FT-IR spectrometer with KBr pellets. Nitrogen adsorption/desorption measurements were carried out on Micromeritics 2020 analyzer at 77.35 K after the samples were degassed at 350 °C under vacuum. X-ray photoelectron spectroscopy (XPS) was performed using an ESCALab 250 spectrometer with a monochromatic X-ray source (Al Kα $h\nu$ = 1486.6 eV). The UV-vis diffuse reflectance spectra were recorded on a PerkinElmer Lambda 950. The steady-state emission spectra were obtained on a HORIBA FLUOROMAX-4 spectrophotometer. The time-resolved photoluminescence (PL) decay analysis was carried out on an Edinburgh Instrument FLS920 spectrophotometer. The electron paramagnetic resonance (EPR) spectra were obtained using a Bruker 300 EPR spectrometer under room temperature. The Ti content of the samples was determined using inductively coupled plasma (ICP) spectroscopy on a PerkinElmer Optima 3300 DV ICP instrument.

2.4. Photocatalytic experiments

2.4.1. Photocatalytic production of H_2O_2. Typically, the as-synthesized catalyst (40 mg) was added to 50 mL of a mixed solution of water and isopropyl alcohol ($V_w : V_i$ = 9:1) in a quartz glass reactor fitted with a temperature-controlled circulating water device (25 ± 1 °C). Photocatalytic H_2O_2 production was performed under visible-light irradiation (λ > 420 nm) with a 300 W Xenon lamp under air-equilibrated conditions for

120 min. Before the photoreaction, the pH of the above-mentioned mixture was adjusted to pH 3 with H_2SO_4. Subsequently, the system was ultrasonically mixed for 30 minutes and stirred for one hour in the dark.

The concentration of H_2O_2 was determined with a traditional iodometric method.[22,23]

This method involves mixing 0.5 mL each of 0.4 M potassium iodide solution and 0.1 M potassium hydrogen phthalate solution with 1 mL of the sample to be tested before waiting for them to fully react for 20 minutes. The mixed solutions were examined with UV visible spectroscopy.

2.4.2. Durability of catalysts test. The stability of the photocatalysts was examined using recycling tests (four runs). After each run, the photocatalysts were collected by centrifugation and washed three times, and finally dried at a temperature of 60 °C in an oven.

2.5. Photoelectric performance test

The as-synthesized samples were examined for their photoelectrochemical performance using a CHI-660e electrochemical system (China). A standard three-electrode model was adopted, in which the synthesized sample/FTO, standard silver electrode (Ag/AgCl), and Pt line served as the working electrode, reference electrode, and counter electrode, respectively. Na_2SO_4 (0.5 mM) was used as the electrolyte. For the fabrication of the working electrodes, 5 mg of the catalyst sample was dispersed into 500 μL of ethanol. This was followed by addition of 10 μL of Nafion solution. The resulting solution was applied uniformly to a 1.0 cm × 1.0 cm ITO glass electrode and then dried for 6 h at 70 °C. The electrochemical impedance spectroscopy (EIS) spectra and transient photocurrent (I–T) of the prepared catalysts were measured at a stable open circuit potential.

3. Results and discussion

3.1. Morphology and structure

The Ti-SAC/g-C_3N_4 photocatalysts were prepared by pyrolyzing the supramolecular precursors with the titanium atoms, which can effectively avoid the hydrolyzation of $TiCl_3$ and introduce titanium single atoms into the matrix of g-C_3N_4 (Fig. 1(a)). The morphologies and distribution of the elements of the as-synthesized samples were determined using scanning electron microscopy (SEM) and transmission electron microscopy (TEM). The SEM and TEM images of Ti-C_3N_4-100 reveal a curly laminar structure with a number of mesopores, as compared with BCN and g-C_3N_4 and shown in Fig. 1(b), (c), and Fig. S1 (ESI†), respectively. These pores can provide sufficient surface active sites to enhance the photocatalytic efficiency. Individual Ti atoms can be observed as bright spots in the high angle annular dark-field scanning transmission electron microscopy (HAADF-STEM) image, as seen in Fig. 1(d), suggesting that a quantity of single Ti atoms have been embedded in the g-C_3N_4 matrix.[24–27] The concentration of Ti of Ti-C_3N_4-100 is 0.09%, as determined using inductively coupled plasma (ICP) analysis, as seen in Table S1 (ESI†). The elemental mapping of Ti-C_3N_4-100
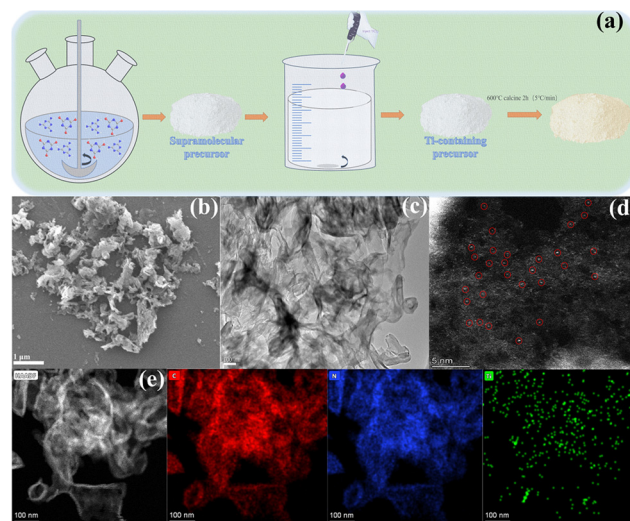

Fig. 1 (a) Schematic illustration of the preparation of Ti-C_3N_4-100. (b) The SEM, (c) TEM, and (d) HAADF-STEM images of Ti-C_3N_4-100. The (e) HAADF-STEM elemental mapping images of Ti-C_3N_4-100.

further illustrates that C, N, Ti atoms are homogeneously distributed in the g-C_3N_4 nanosheets (Fig. 1(e)), consistent with the result of the HAADF-STEM.

The X-ray diffraction (XRD) patterns of BCN, g-C_3N_4 and the Ti-SAC/g-C_3N_4 with different Ti contents are shown in Fig. 2(a). All the patterns demonstrate two characteristic peaks at 13.1° and 27.1°, respectively, which can be attributed to the typical diffraction peaks of g-C_3N_4 (PDF#50-1250). The first one is related to the in-plane ordering of repetitive heptazine units, corresponding to (100).[28] The second one is associated with the interlayer stacking of conjugated aromatic ring lamellar stacking of the graphite phase, ascribed to (200).[29] In contrast to BCN, the (002) peak of the g-C_3N_4 shows an obvious
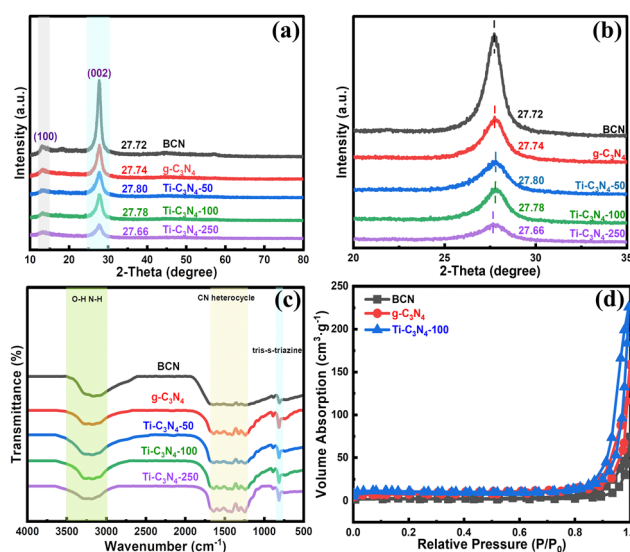

Fig. 2 (a) and (b) XRD patterns and (c) FTIR spectra of each sample. (d) The N_2 adsorption–desorption isotherms of BCN, g-C_3N_4 and Ti-C_3N_4-100.

hypochromatic shift owing to the increase of the interlayer distance, as shown in Fig. 2(b).[16] The Ti-SAC/g-C$_3$N$_4$ samples exhibit different experimental results. The (002) peaks of Ti-C$_3$N$_4$-50 and Ti-C$_3$N$_4$-100 present slight bathochromic shifts in contrast to g-C$_3$N$_4$, which can be attributed to the shrinkage of the carbon nitride lattice due to Ti doping. However, the (002) peak of Ti-C$_3$N$_4$-250 presents a slight hypsochromic shift relative to g-C$_3$N$_4$, as the concentration of titanium is further increased. This indicates that further doping can give rise to the expansion of the lattice. No pure TiO$_2$ crystal phases can be detected for the Ti-SAC/g-C$_3$N$_4$ photocatalysts, implying that the titanium atoms have been embedded in the C$_3$N$_4$ matrix, consistent with the HAADF-STEM results.

To investigate the surface groups, the Fourier-transform infrared (FTIR) spectra were obtained (Fig. 2(c)). The absorption bands of the Ti-SAC/g-C$_3$N$_4$ photocatalysts are similar to that of pure bulk g-C$_3$N$_4$, according to previous reports, indicating that the introduction of titanium atoms cannot change the surface composition and structure of g-C$_3$N$_4$. The vibration bands at 1200–1700 cm^{-1} should be attributed to the aromatic C–N stretching mode of the heterocycles.[30] The vibration peak centered at 806 cm^{-1} corresponds to the respiratory mode of tri-s-triazine in C$_3$N$_4$.[31] The broad absorption band in the range 3000–3400 cm^{-1} can be ascribed to the typical N–H and O–H vibrations of uncondensed amino groups and adsorbed water molecules.[32] respectively.

The nitrogen adsorption–desorption isotherm of the calcined BCN, g-C$_3$N$_4$ and Ti-C$_3$N$_4$-100 exhibit a type IV isotherm with an H$_3$ hysteresis loop, confirming the existence of mesopores, as shown in Fig. 2(d).[33] The Brunauer–Emmett–Teller (BET) surface area of Ti-C$_3$N$_4$-100 is calculated to be 32.98 m^2 g^{-1}, which is larger than that of BCN (4.73 m^2 g^{-1}) and g-C$_3$N$_4$ (24.98 m^2 g^{-1}), as seen in Table S2 (ESI†). The pore volume of Ti-C$_3$N$_4$-100 obtained from the N$_2$ adsorption volumes at the specific point ($P/P_0 = 0.99$) is 0.35 cm^3 g^{-1}, higher than that of BCN (0.11 cm^3 g^{-1}) and g-C$_3$N$_4$ (0.17 cm^3 g^{-1}), as shown in Table S2 and Fig. S2 (ESI†). This observation can be ascribed to the introduction of titanium, which can lead to an increase in the number of structural defects and active edges in the melon units and further results in an increase of the surface area and pore volume This result suggests that single titanium atoms can facilitate the formation of a mesoporous structure during polycondensation.[34]

To further confirm the elemental distribution and chemical states of Ti-C$_3$N$_4$-100, X-ray photoelectron (XPS) characterization was performed. Fig. S3 (ESI†) exhibits the XPS spectra of C, N and Ti for BCN, g-C$_3$N$_4$ and Ti-C$_3$N$_4$-100. The C 1s peaks of BCN and g-C$_3$N$_4$ are doublets with binding energies of 284.8 eV, 288.3 eV and 284.8 eV, 288.3 eV, corresponding to the surface contaminated carbon (C–C/C=C) and the sp^2 hybrid carbon of the triazine ring (N–C=N)[35,36] (Fig. S3b, ESI†). However, the C 1s peaks of Ti-C$_3$N$_4$-100 are triplets with binding energies of 284.8 eV, 288.2 eV and 286.5 eV. The first two peaks can be attributed to the surface contaminated carbon (C–C/C=C) and the sp^2 hybrid carbon of the triazine ring (N–C=N), consistent with BCN and g-C$_3$N$_4$. The third peak confirms the existence of

C–O bonds in the Ti-C$_3$N$_4$-100 sample.[37] Meanwhile, the N 1s peaks of BCN and g-C$_3$N$_4$ are triplets with binding energies of 398.7 eV, 399.4 eV, 401.3 eV and 398.4 eV, 399.2 eV, 401.2 eV (Fig. S3c, ESI†), which are attributed to the sp^2 nitrogen in the triazine rings (C–N=C), tertiary nitrogen (N–(C)$_3$), and C–NH$_x$.[38,39] The introduction of titanium shifts the N 1s peaks to 398.4 eV, 399.6 eV, and 400.9 eV, which demonstrates that the binding energy of 399.6 eV in Ti-C$_3$N$_4$-100 is obviously higher than that of BCN and g-C$_3$N$_4$. The shift in the binding energies of the N elements implies that the titanium atoms in Ti-C$_3$N$_4$-100 can interacted with the N atoms, confirming the formation of N–Ti bonds. The XPS spectrum of the Ti 2p peaks are not obviously visible due to low concentration, as shown by the ICP results (Fig. S3d, ESI†).

3.2. Photocatalytic performance

The photocatalytic performance strongly depends on the Ti concentration in the Ti-SAC/g-C$_3$N sample used for H$_2$O$_2$ production (Fig. 3(a)). It is obvious that the photocatalytic activity of the Ti-SAC/g-C$_3$N$_4$ photocatalysts is higher than that of BCN and g-C$_3$N$_4$. The photocatalytic activity cannot be promoted until the concentration of the Ti atom reaches 0.09%. Ti-C$_3$N$_4$-100 shows the best photocatalytic performance and the H$_2$O$_2$ production rate can reach 356.45 μmol L^{-1} h^{-1}, being 2.24 and 2.13 times higher than that of BCN and g-C$_3$N$_4$, respectively. The photocatalytic efficiency decrease at higher concentrations of Ti, which can be attributed to the decrease of the conduction band edge, as shown in our pervious report.[40] The above-mentioned results suggest that the single atom Ti doping concentration can control the photocatalytic activity of the Ti-SAC/g-C$_3$N$_4$ material. Furthermore, recyclability experiments were performed with Ti-C$_3$N$_4$-100, whereby the catalyst was recovered using centrifugal separation and then reused in a four cycle run of further experiments (Fig. 3(b)). No significant changes in the crystal structure and chemical composition can be observed after four successive runs, confirming the excellent stability of the Ti-SAC/g-C$_3$N$_4$ photocatalysts (Fig. S4, ESI†). Furthermore, the H$_2$O$_2$ production rate of Ti-C$_3$N$_4$-100 is higher than that of other C$_3$N$_4$-based photocatalysts (Table 1), indicating that the Ti-SAC/C$_3$N$_4$ photocatalysts are promising photocatalysts for H$_2$O$_2$ production.
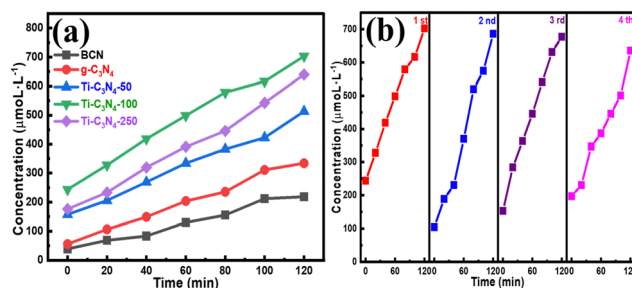

Fig. 3 (a) The photocatalytic hydrogen peroxide production performance of each sample. (b) Recycling performance of Ti-C$_3$N$_4$-100 photocatalyst.

Table 1 Comparison of H_2O_2 production with different photocatalysts

System	Dosage (g L^{-1})	Production (μM g^{-1} h^{-1})	Ref.
DCN	0.83	96.80	23
OCN	1.00	1200.0	41
g-C_3N_4	4.00	125.0	7
CoP/CN	1.00	3200.0	42
CdS-GO	1.67	2560.0	43
ZnO/WO$_3$	1.00	6788.00	44
Ti-C_3N_4-100	0.4	8911.25	

3.3. Photocatalytic mechanism

To further investigate the effects of single Ti atom-doping, the PL spectra, EIS spectra were obtained and relative photoelectrochemical experiments were conducted. Fig. 4(a) shows that doping with titanium atoms can effectively reduce the PL intensity, indicating that the doping of single titanium atoms can promote electron–hole pair separation and efficient charge transfer.[45] Subsequently, the time-resolved PL spectra were obtained to further verify the above-mentioned PL results (Fig. 4(b)). The average lifetime of Ti-C_3N_4-100 is significantly shorter than that of the BCN and g-C_3N_4, as shown in Table S3 (ESI†). This result suggests that the reduction of the excited state can take place by means of a non-radiative pathway, possibly through electron charge transfer to some advantageous defect states, thus further increasing charge transfer and separation.[46] Fig. 4(c) shows that the photo-generated current density of Ti-C_3N_4-100 is obviously higher than that of BCN and g-C_3N_4, confirming the high efficiency of charge separation and transfer.[47] In addition, the EIS spectra show that the diameter of the semicircles of Ti-C_3N_4-100 is the smallest of all the photocatalysts (Fig. 4(d)). This demonstrates that single Ti atom-doping is beneficial for photo-generated electron–hole

pair separation and charge transfer,[48] consistent with the PL and photoelectrochemical results.

To analyse in depth the mechanism of photocatalytic enhancement of Ti-SAC/g-C_3N_4, the absorption spectra of all samples were evaluated using ultraviolet-visible diffuse reflectance spectroscopy (UV-Vis DRS). Fig. 5(a) shows that the Ti-SAC/g-C_3N_4 photocatalysts have stronger absorption intensities in the ultraviolet and visible light region than BCN and g-C_3N_4. The absorption edges of the Ti-SAC/g-C_3N_4 photocatalysts are bathochromically shifted in contrast to those of BCN and g-C_3N_4, indicating that the introduction of single titanium atoms can effectively modulate the structure of the energy band.[40] In addition, the optical band gaps can be calculated in accordance with the Kubelka–Munk equation (Fig. 5(a) inset). The result indicates that the energy bandgaps (E_g) of the Ti-SAC/g-C_3N_4 photocatalysts are smaller than those of BCN (2.74 eV) and g-C_3N_4 (2.80 eV). E_g gradually decreases as the amount of TiCl$_3$ is increased to 100 μL, and slightly increases as the amount of TiCl$_3$ is further increased to 250 μL. The conduction band (CB) energies are determined using Mott–Schottky curves (MS) to investigate the effect that titanium single atoms have on the C_3N_4 matrix (Fig. 5(b)). Subsequently, the valence band (VB) potential of all photocatalysts were determined in agreement with the empirical formula (VB = CB + E_g) (Fig. 5(c)). The CB
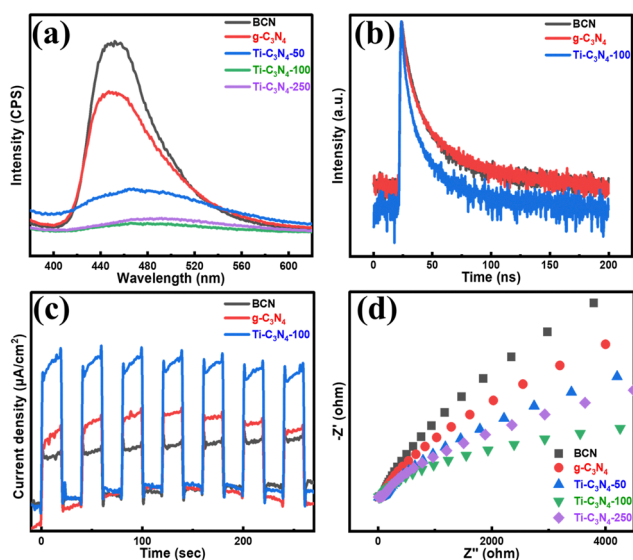
Fig. 4 (a) PL spectra of BCN, g-C_3N_4 and Ti-C_3N_4-100, (b) time-resolved PL spectra of BCN, g-C_3N_4 and Ti-C_3N_4-100, (c) photocurrent response, and (d) EIS spectra of BCN, g-C_3N_4 and Ti-C_3N_4-100.
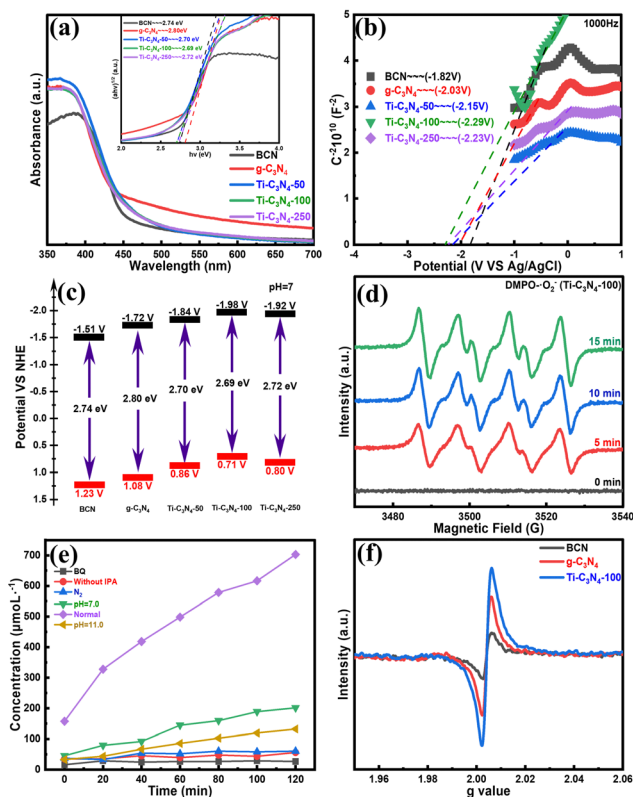
Fig. 5 (a) UV-vis diffuse reflectance spectra and band gap (higher-middle inset), (b) Mott−Schottky plots and (c) electronic band structures of all samples. (d) ESR spectrum of DMPO-•O_2^- in the presence of Ti-C_3N_4-100, (e) photocatalytic performance of Ti-C_3N_4-100 under different conditions, and (f) EPR spectra of BCN, g-C_3N_4 and Ti-C_3N_4-100.
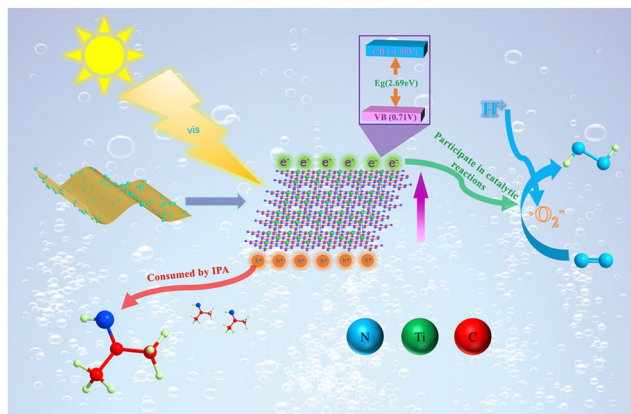
Fig. 6 Proposed photocatalytic mechanism for the Ti-C$_3$N$_4$-100 photocatalyst.

potentials of CB the Ti-SAC/g-C$_3$N$_4$ photocatalysts reveal a volcanic tendency, being more negative than that of g-C$_3$N$_4$. The CB potential is correlated with the production of photogenerated electrons, combining with O$_2$ to generate superoxide radicals. The superoxide radicals have an effect on the H$_2$O$_2$ production rate. The more negative the CB potential is, the higher the H$_2$O$_2$ production rate is. This result is observed by analyzing the concentration of single titanium atoms and the photocatalytic performance. Furthermore, the photogenerated holes can be fully consumed due to the presence of isopropyl alcohol, which facilitates the smooth progress of the 2-electron reaction of oxygen. Thus, it can be seen that varying the concentration of single titanium atoms can modulate the energy band structure and the light harvesting ability of the Ti-SAC/g-C$_3$N$_4$ photocatalysts.

Subsequently, a series of experiments were performed to further investigate the process of photocatalytic H$_2$O$_2$ production, confirming the primary photocatalytic active species. The ESR spectra exhibit the existence of superoxide radicals when 5,5-dimethyl-1-pyrroline *N*-oxide (DMPO) is employed as the scavenging agent (Fig. 5(d)). No DMPO-$^{\bullet}$O$_2^-$ peaks could be obtained in the dark. However, the significant signals of DMPO-$^{\bullet}$O$_2^-$ can be observed with the presence of Ti-C$_3$N$_4$-100 under visible light illumination. Next, radical capture experiments show that BQ obviously decrease the activity of Ti-C$_3$N$_4$-100, determining the predominant role of the superoxide radicals. Meanwhile, the decomposition of H$_2$O$_2$ can be inhibited owing to the presence of IPA. In addition, no H$_2$O$_2$ can be produced in an N$_2$ atmosphere, indicating that the presence of O$_2$ is required. The above-mentioned results expressly suggest that the formation of superoxide radicals is vital for the production of H$_2$O$_2$ (Fig. 5(e)), which is consistent with previous reports. Furthermore, the adsorption of O$_2$ is another important factor for the production of H$_2$O$_2$ due to the low concentration of O$_2$ in water. The electron paramagnetic resonance (EPR) spectra show that Ti-C$_3$N$_4$-100 exhibits a stronger EPR response than BCN and g-C$_3$N$_4$ (Fig. 5(f)), which leads to the adsorption of more O$_2$ molecules by Ti-C$_3$N$_4$-100 than by the BCN and g-C$_3$N$_4$ reaction systems. These results demonstrate

that doping single titanium atoms is not only beneficial to the delocalization of heptazine π-conjugated rings, resulting in a high mobility of charge transfer and separation, but also improves the adsorption of O$_2$ molecules.[49] The synergy of the two sides together promotes the photocatalytic effect of Ti-C$_3$N$_4$-100.

A possible photocatalytic mechanism for the Ti-SAC/g-C$_3$N$_4$ photocatalysts can be proposed on the basis of the above results (Fig. 6). Firstly, the introduction of single titanium atoms further reduces the band gap of C$_3$N$_4$, increasing the absorption of visible light. Secondly, the doping of the appropriate quantity of single titanium atoms can not only lead to a more negative CB, improving the reducing ability of the photocatalysts, but can also increase the adsorption of O$_2$ molecules in solution by Ti-SAC/g-C$_3$N$_4$. Thirdly, the photoinduced electrons are helpful for the formation of superoxide radicals, promoting the production of H$_2$O$_2$. Meanwhile, the photoinduced holes can be eliminated by IPA, decreasing the decomposition of H$_2$O$_2$. The photocatalytic process of H$_2$O$_2$ production can be summarized as follows:[50]

$$O_2 + e^- \rightarrow O_2^- \tag{1}$$

$$O_2^- + 2H^+ + e^- \rightarrow H_2O_2 \tag{2}$$

$$O_2 + 2e^- + 2H^+ \rightarrow H_2O_2 \tag{3}$$
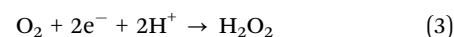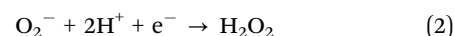
4. Conclusions

Ti-SAC/g-C$_3$N$_4$ photocatalysts have been prepared by using TiCl$_3$ as the titanium source, owing to its excellent chemical stability in solution, to embed single titanium atoms into a C$_3$N$_4$ matrix. The photocatalytic activity experiments demonstrate that the Ti-C$_3$N$_4$-100 sample has the best catalytic performance. The H$_2$O$_2$ production rate can reach 356.45 μmol L^{-1} h^{-1}, which is 2.44 and 2.13 times higher than BCN and g-C$_3$N$_4$, respectively. Further investigations demonstrate that the bottom of the conduction band (CB) and the maximum of the valence band (VB) can be controlled by varying the concentration of titanium atoms. The Ti-C$_3$N$_4$-100 sample has a concentration of 0.09% titanium and possesses the highest bottom of the CB and the highest maximum of the VB. The more negative the bottom of the CB is, the better the photocatalytic efficiency is. This study demonstrates that superoxide radicals can be easily generated when the bottom of the CB is negative, and the generation of superoxide radicals is crucial to the photocatalytic process. In addition, the doping of single titanium atoms can also form vacancies to enhance the adsorption of the O$_2$ molecules. These results provide a distinctive strategy to realize single atom-doping of titanium and offers new insights into the structure–property relationship.

Conflicts of interest

There are no conflicts to declare

Acknowledgements

Notes and references

1 J. M. Campos-Martin, G. Blanco-Brieva and J. L. Fierro, Hydrogen peroxide synthesis: an outlook beyond the anthraquinone process, *Angew. Chem., Int. Ed.*, 2006, **45**, 6962–6984.

2 D. Tsukamoto, A. Shiro, Y. Shiraishi, Y. Sugano, S. Ichikawa, S. Tanaka and T. Hirai, Photocatalytic H_2O_2 Production from ethanol/O_2 system using TiO_2 loaded with Au–Ag bimetallic alloy nanoparticles, *ACS Catal.*, 2012, **2**, 599–603.

3 J. Liu, Y. Zou, D. Cruz, A. Savateev, M. Antonietti and G. Vile, Ligand-Metal charge transfer induced *via* adjustment of textural properties controls the performance of single-atom catalysts during photocatalytic Degradation, *ACS Appl. Mater. Interfaces*, 2021, **13**, 25858–25867.

4 Y. Yang, Z. Zeng, G. Zeng, D. Huang, R. Xiao, C. Zhang, C. Zhou, W. Xiong, W. Wang, M. Cheng, W. Xue, H. Guo, X. Tang and D. He, Ti_3C_2 Mxene/porous g-C_3N_4 interfacial Schottky junction for boosting spatial charge separation in photocatalytic H_2O_2 production, *Appl. Catal., B*, 2019, **258**, 7956–7965.

5 X. Zhao, Y. You, S. Huang, Y. Wu, Y. Ma, G. Zhang and Z. Zhang, Z-scheme photocatalytic production of hydrogen peroxide over $Bi_4O_5Br_2$/g-C_3N_4 heterostructure under visible light, *Appl. Catal., B*, 2020, **278**, 9251–9261.

6 Y. Zhang, C. Pan, G. Bian, J. Xu, Y. Dong, Y. Zhang, Y. Lou, W. Liu and Y. Zhu, H_2O_2 generation from O_2 and H_2O on a near-infrared absorbing porphyrin supramolecular photocatalyst, *Nat. Energy*, 2023, **8**, 361–371.

7 Y. Shiraishi, S. Kanazawa, Y. Sugano, D. Tsukamoto, H. Sakamoto, S. Ichikawa and T. Hirai, Highly Selective Production of Hydrogen Peroxide on Graphitic Carbon Nitride (g-C_3N_4) Photocatalyst Activated by Visible Light, *ACS Catal.*, 2014, **4**, 774–780.

8 A. Asghar, A. A. Abdul Raman and W. M. A. Wan Daud, Advanced oxidation processes for in-situ production of hydrogen peroxide/hydroxyl radical for textile wastewater treatment: a review, *J. Cleaner Prod.*, 2015, **87**, 826–838.

9 L. Zheng, H. Su, J. Zhang, L. S. Walekar, H. Vafaei Molamahmood, B. Zhou, M. Long and Y. H. Hu, Highly selective photocatalytic production of H_2O_2 on sulfur and nitrogen co-doped graphene quantum dots tuned TiO_2, *Appl. Catal., B*, 2018, **239**, 475–484.

10 H. Hou, X. Zeng and X. Zhang, Production of Hydrogen Peroxide by Photocatalytic Processes, *Angew. Chem., Int. Ed.*, 2020, **59**, 17356–17376.

11 J. Fu, J. Yu, C. Jiang and B. Cheng, g-C_3N_4-Based Heterostructured Photocatalysts, *Adv. Energy Mater.*, 2018, **8**, 1503–1533.

12 M. Jourshabani, M. R. Asrami and B.-K. Lee, An efficient and unique route for the fabrication of highly condensed oxygen-doped carbon nitride for the photodegradation of synchronous pollutants and H_2O_2 production under ambient conditions, *Appl. Catal., B*, 2022, **302**, 839–852.

13 R. Tang, D. Gong, Y. Zhou, Y. Deng, C. Feng, S. Xiong, Y. Huang, G. Peng and L. Li, Unique g-C_3N_4/PDI-g-C_3N_4 homojunction with synergistic piezo-photocatalytic effect for aquatic contaminant control and H_2O_2 generation under visible light, *Appl. Catal., B*, 2022, **303**, 120929.

14 Y. Wang, J. Mao, X. Meng, L. Yu, D. Deng and X. Bao, Catalysis with Two-Dimensional Materials Confining Single Atoms: Concept, Design, and Applications, *Chem. Rev.*, 2019, **119**, 1806–1854.

15 L. Zhang, R. Long, Y. Zhang, D. Duan, Y. Xiong, Y. Zhang and Y. Bi, Direct Observation of Dynamic Bond Evolution in Single-Atom Pt/$C_{(3)}N_{(4)}$ Catalysts, *Angew. Chem., Int. Ed.*, 2020, **59**, 6224–6229.

16 X. Xiao, Y. Gao, L. Zhang, J. Zhang, Q. Zhang, Q. Li, H. Bao, J. Zhou, S. Miao, N. Chen, J. Wang, B. Jiang, C. Tian and H. Fu, A Promoted Charge Separation/Transfer System from Cu Single Atoms and $C_{(3)}N_{(4)}$ Layers for Efficient Photocatalysis, *Adv. Mater.*, 2020, **32**, e2003082.

17 Y. Wang, X. Zhao, D. Cao, Y. Wang and Y. Zhu, Peroxymonosulfate enhanced visible light photocatalytic degradation bisphenol A by single-atom dispersed Ag mesoporous g-C_3N_4 hybrid, *Appl. Catal., B*, 2017, **211**, 79–88.

18 Q. Dai, S. Bai, J. Wang, M. Li, X. Wang and G. Lu, The effect of TiO_2 doping on catalytic performances of Ru/CeO_2 catalysts during catalytic combustion of chlorobenzene, *Appl. Catal., B*, 2013, **142–143**, 222–233.

19 S. Zhou, Y. Liu, J. Li, Y. Wang, G. Jiang, Z. Zhao, D. Wang, A. Duan, J. Liu and Y. Wei, Facile in situ synthesis of graphitic carbon nitride (g-C_3N_4)-N-TiO_2 heterojunction as an efficient photocatalyst for the selective photoreduction of CO_2 to CO, *Appl. Catal., B*, 2014, **158–159**, 20–29.

20 T. Cai, L. Wang, Y. Liu, S. Zhang, W. Dong, H. Chen, X. Yi, J. Yuan, X. Xia, C. Liu and S. Luo, Ag_3PO_4/Ti_3C_2 MXene interface materials as a Schottky catalyst with enhanced photocatalytic activities and anti-photocorrosion performance, *Appl. Catal., B*, 2018, **239**, 545–554.

21 X. Bao, H. Li, Z. Wang, F. Tong, M. Liu, Z. Zheng, P. Wang, H. Cheng, Y. Liu, Y. Dai, Y. Fan, Z. Li and B. Huang, TiO_2/Ti_3C_2 as an efficient photocatalyst for selective oxidation of benzyl alcohol to benzaldehyde, *Appl. Catal., B*, 2021, **286**, 9885–9894.

22 Y. Yang, G. Zeng, D. Huang, C. Zhang, D. He, C. Zhou, W. Wang, W. Xiong, X. Li, B. Li, W. Dong and Y. Zhou, Molecular engineering of polymeric carbon nitride for highly efficient photocatalytic oxytetracycline degradation and H_2O_2 production, *Appl. Catal., B*, 2020, **272**, 8970–8983.

23 Z. Wei, M. Liu, Z. Zhang, W. Yao, H. Tan and Y. Zhu, Efficient visible-light-driven selective oxygen reduction to hydrogen peroxide by oxygen-enriched graphitic carbon nitride polymers, *Energy Environ. Sci.*, 2018, **11**, 2581–2589.

24 B. Wu, R. Yang, L. Shi, T. Lin, X. Yu, M. Huang, K. Gong, F. Sun, Z. Jiang, S. Li, L. Zhong and Y. Sun, Cu single-atoms embedded in porous carbon nitride for selective oxidation of methane to oxygenates, *Chem. Commun.*, 2020, **56**, 14677–14680.

25 H. Li, B. Zhu, B. Cheng, G. Luo, J. Xu and S. Cao, Single-atom Cu anchored on N-doped graphene/carbon nitride heterojunction for enhanced photocatalytic H_2O_2 production, *J. Mater. Sci. Technol.*, 2023, **161**, 192–200.

26 C. Zhou, Y. Liang, W. Xia, E. Almatrafi, B. Song, Z. Wang, Y. Zeng, Y. Yang, Y. Shang, C. Wang and G. Zeng, Single atom Mn anchored on N-doped porous carbon derived from spirulina for catalyzed peroxymonosulfate to degradation of emerging organic pollutants, *J. Hazard. Mater.*, 2023, **441**, DOI: 10.1016/j.jhazmat.2022.129871.

27 G. Feng, H. Huang, M. Zhang, Z. Wu, D. Sun, Q. Chen, D. Yang, Y. Zheng, Y. Chen and X. Jing, Single Atom Iron-Doped Graphic-Phase C_3N_4 Semiconductor Nanosheets for Augmented Sonodynamic Melanoma Therapy Synergy with Endowed Chemodynamic Effect, *Adv. Sci.*, 2023, **10**, DOI: 10.1002/advs.202302579.

28 W. J. Ong, L. L. Tan, Y. H. Ng, S. T. Yong and S. P. Chai, Graphitic Carbon Nitride (g-C_3N_4)-Based Photocatalysts for Artificial Photosynthesis and Environmental Remediation: Are We a Step Closer To Achieving Sustainability?, *Chem. Rev.*, 2016, **116**, 7159–7329.

29 H. Shi, G. Chen, C. Zhang and Z. Zou, Polymeric g-C_3N_4 Coupled with $NaNbO_3$ Nanowires toward Enhanced Photocatalytic Reduction of CO_2 into Renewable Fuel, *ACS Catal.*, 2014, **4**, 3637–3643.

30 Y. Jiang, Z. Sun, C. Tang, Y. Zhou, L. Zeng and L. Huang, Enhancement of photocatalytic hydrogen evolution activity of porous oxygen doped g-C_3N_4 with nitrogen defects induced by changing electron transition, *Appl. Catal., B*, 2019, **240**, 30–38.

31 X. Bai, L. Wang, Y. Wang, W. Yao and Y. Zhu, Enhanced oxidation ability of g-C_3N_4 photocatalyst via C_{60} modification, *Appl. Catal., B*, 2014, **152–153**, 262–270.

32 H. Wang, Y. Xu, D. Xu, L. Chen, X. Qiu and Y. Zhu, Graphitic Carbon Nitride for Photoelectrochemical Detection of Environmental Pollutants, *ACS ES&T Engg*, 2022, **2**, 140–157.

33 J. Xie, C. Wang, N. Chen, W. Chen, J. Xu, P. Bai, B. Liu, L. Zhang and H. Wang, Highly active g-C_3N_4 photocatalysts modified with transition metal cobalt for hydrogen evolution, *J. Mater. Chem. C*, 2021, **9**, 4378–4384.

34 F. He, S. Wang, H. Zhao, Y. Wang, J. Zhang, Q. Yan, P. Dong, Z. Tai, L. Chen, Y. Wang and C. Zhao, Construction of Schottky-type Ag-loaded fiber-like carbon nitride photocatalysts for tetracycline elimination and hydrogen evolution, *Appl. Surf. Sci.*, 2019, **485**, 70–80.

35 X. Zhang, P. Ma, C. Wang, L. Gan, X. Chen, P. Zhang, Y. Wang, H. Li, L. Wang, X. Zhou and K. Zheng, Unraveling the dual defect sites in graphite carbon nitride for ultra-high photocatalytic H_2O_2 evolution, *Energy Environ. Sci.*, 2022, **15**, 830–842.

36 H. Li, S. Gan, H. Wang, D. Han and L. Niu, Intercorrelated Superhybrid of AgBr Supported on Graphitic-C_3N_4-Decorated Nitrogen-Doped Graphene: High Engineering Photocatalytic Activities for Water Purification and CO_2 Reduction, *Adv. Mater.*, 2015, **27**, 6906–6913.

37 F. Wei, Y. Liu, H. Zhao, X. Ren, J. Liu, T. Hasan, L. Chen, Y. Li and B. L. Su, Oxygen self-doped g-$C_{(3)}N_{(4)}$ with tunable electronic band structure for unprecedentedly enhanced photocatalytic performance, *Nanoscale*, 2018, **10**, 4515–4522.

38 J. Zhang, M. Zhang, C. Yang and X. Wang, Nanospherical carbon nitride frameworks with sharp edges accelerating charge collection and separation at a soft photocatalytic interface, *Adv. Mater.*, 2014, **26**, 4121–4126.

39 Q. Han, B. Wang, Y. Zhao, C. Hu and L. Qu, A Graphitic-C_3N_4 ''Seaweed'' Architecture for Enhanced Hydrogen Evolution, *Angew. Chem., Int. Ed.*, 2015, **54**, 11433–11437.

40 J. Xin, F. Li, Z. Li, J. Zhao and Y. Wang, Controlling the band structure and photocatalytic performance of single atom Ag/C_3N_4 catalysts by variation of silver concentration, *Inorg. Chem. Front.*, 2022, **9**, 302–309.

41 L. Shi, L. Yang, W. Zhou, Y. Liu, L. Yin, X. Hai, H. Song and J. Ye, Photoassisted Construction of Holey Defective g-$C_{(3)}N_{(4)}$ Photocatalysts for Efficient Visible-Light-Driven $H_{(2)}O_{(2)}$ Production, *Small*, 2018, **14**, 3142–3150.

42 Y. Peng, L. Wang, Y. Liu, H. Chen, J. Lei and J. Zhang, Visible-Light-Driven photocatalytic H_2O_2 production on g-C_3N_4 loaded with CoP as a noble metal free cocatalyst, *Eur. J. Inorg. Chem.*, 2017, 4797–4802.

43 S. Thakur, T. Kshetri, N. H. Kim and J. H. Lee, Sunlight-driven sustainable production of hydrogen peroxide using a CdS–graphene hybrid photocatalyst, *J. Catal.*, 2017, **345**, 78–86.

44 Z. Jiang, B. Cheng, Y. Zhang, S. Wageh, A. A. Al-Ghamdi, J. Yu and L. Wang, S-scheme ZnO/WO_3 heterojunction photocatalyst for efficient H_2O_2 production, *J. Mater. Sci. Technol.*, 2022, **124**, 193–201.

45 B. Lin, G. Yang and L. Wang, Stacking-Layer-Number Dependence of Water Adsorption in 3D Ordered Close-Packed g-$C_{(3)}N_{(4)}$ Nanosphere Arrays for Photocatalytic Hydrogen Evolution, *Angew. Chem., Int. Ed.*, 2019, **58**, 4587–4591.

46 Y. Tian, L. Zhou, Q. Zhu, J. Lei, L. Wang, J. Zhang and Y. Liu, Hierarchical macro-mesoporous g-$C_{(3)}N_{(4)}$ with an inverse opal structure and vacancies for high-efficiency solar energy conversion and environmental remediation, *Nanoscale*, 2019, **11**, 20638–20647.

47 B. Lin, S. Chen, F. Dong and G. Yang, A ball-in-ball g-$C(3)N(4)@SiO_{(2)}$ nano-photoreactor for highly efficient $H_{(2)}$ generation and NO removal, *Nanoscale*, 2017, **9**, 5273–5279.

48 B. Ma, G. Chen, C. Fave, L. Chen, R. Kuriki, K. Maeda, O. Ishitani, T. C. Lau, J. Bonin and M. Robert, Efficient Visible-Light-Driven $CO_{(2)}$ Reduction by a Cobalt Molecular Catalyst Covalently Linked to Mesoporous Carbon Nitride, *J. Am. Chem. Soc.*, 2020, **142**, 6188–6195.

49 Y. Cui, Z. Ding, X. Fu and X. Wang, Construction of conjugated carbon nitride nanoarchitectures in solution at low temperatures for photoredox catalysis, *Angew. Chem., Int. Ed.*, 2012, **51**, 11814–11818.

50 S. Li, G. Dong, R. Hailili, L. Yang, Y. Li, F. Wang, Y. Zeng and C. Wang, Effective photocatalytic H_2O_2 production under visible light irradiation at g-C_3N_4 modulated by carbon vacancies, *Appl. Catal., B*, 2016, **190**, 26–35.